




Comparative study of phase structure, dielectric properties and electrocaloric effect in novel high-entropy ceramics

Wei Liu^{1,2}, Feng Li^{2,*} , Guohua Chen³, Guohui Li⁴, Hongwei Shi², Li Li¹, Youmin Guo¹, Jiwei Zhai⁴, and Chunchang Wang^{1,*}

¹Laboratory of Dielectric Functional Materials, School of Physics & Materials Science, Anhui University, Hefei 230601, China

²Information Materials and Intelligent Sensing Laboratory of Anhui Province, Institutes of Physical Science and Information Technology, Anhui University, Hefei 230601, China

³Guangxi Key Laboratory of Information Materials, Guilin University of Electronic Technology, Guilin 541004, China

⁴School of Materials Science & Engineering, Tongji University, 4800 Caoan road, Shanghai 201804, China

Received: 4 June 2021

Accepted: 13 September 2021

Published online:

22 September 2021

© The Author(s), under exclusive licence to Springer Science+Business Media, LLC, part of Springer Nature 2021

ABSTRACT

Unique structure and performance in prominent high-entropy ceramics (HECs) have attracted enormous attentions recently. In this work, we have successfully synthesized pure-phase $(\text{Bi}_{1/6}\text{Na}_{1/6}\text{Sr}_{1/6}\text{Ba}_{1/6}\text{Pb}_{1/6}\text{Ca}_{1/6})\text{TiO}_3$ (BNSBPC) and $(\text{Bi}_{1/6}\text{La}_{1/6}\text{Na}_{1/6}\text{K}_{1/6}\text{Sr}_{1/6}\text{Ba}_{1/6})\text{TiO}_3$ (BLNKSb) HECs by conventional solid-state method. Rietveld refinement results show that BNSBPC composition possesses tetragonal phase ($P4mm$) while the BLNKSb one exhibits cubic phase ($Pm\bar{3}m$). Dielectric characterization reveals distinct relaxation behaviors between BNSBPC and BLNKSb compositions. Relaxor-like nature in BNSBPC and Debye medium in BLNKSb one are verified by dielectric, ferroelectric and Raman spectra characterizations. Maximal electrocaloric effect (ECE, ΔT_{max}) reaches 0.63 K with relatively narrow temperature span (ΔT_{span}) of ~ 20 K at 60 kV cm^{-1} for BNSBPC ceramic, while the BLNKSb one possesses superior temperature stability ($\Delta T_{span} = 100$ K) with $\Delta T_{max} = 0.14$ K. Room-temperature ECE is also obtained by home-made adiabatic calorimeter, which indicates a positive ECE for both compositions. Finally, phase structure, dielectric properties and ECE in two high-entropy compositions are comparatively discussed to explore structure–ECE relationships in HECs. The superior thermal stability of ECE in BLNKSb samples provides a broad prospect for designing solid-state refrigeration.

Handling Editor: David Cann.

Address correspondence to E-mail: fengli@ahu.edu.cn; ccwang@ahu.edu.cn

<https://doi.org/10.1007/s10853-021-06530-9>

Introduction

Conventional compression refrigeration devices have disadvantages of complex structure, large volume and low efficiency with production of greenhouse gas, which retards a progress of integrations, miniaturizations and creation of environment-friendly society [1]. To overcome these shortcomings, solid-state refrigeration technology has stepped onto the stage of history. This technology is based on the electrocaloric effect (ECE), which is defined as temperature variation in polar materials with application and removal of electric field [2]. Since it has merits of easy miniaturization, low cost/noise and high efficiency, it gradually becomes a promising candidate in application of refrigeration devices. After years of silence, Mischenko et al. reported a large adiabatic temperature change (ΔT) of 12 K in $\text{PbZr}_{0.95}\text{Ti}_{0.05}\text{O}_3$ thin films, thus igniting passions in exploring novel material with a large ECE [3]. Taking heat-transfer efficiency into account, high-ECE researches in bulk materials are mainstream, both lead-containing such as $\text{Pb}(\text{Mg}_{1/3}\text{Nb}_{2/3})\text{O}_3$ - PbTiO_3 (PMN-PT) [4, 5] and lead-free ceramics such as BaTiO_3 - (BT) [6–12], $\text{K}_{0.5}\text{Na}_{0.5}\text{NbO}_3$ - (KNN) [13–15], NaNbO_3 - (NN) [16, 17] and $\text{Bi}_{0.5}\text{Na}_{0.5}\text{TiO}_3$ -based (BNT) [18–20]. However, there are some weakness that hiding behind excellent performances. For instance, lead-containing ceramics have a high ECE but are not friendly to the environment. BT bulk ceramics produce large ΔT under electric field, the maximal ECE deviates from room temperature with narrow working temperature range yet. Ferroelectric-relaxor phase transition boosts ECE in BNT-based ceramics. However, the contribution of polar nanoregions (PNRs) leads to temperature instability. When modulating the transition temperature near room temperature, temperature stability has been improved. However, ECE peak value is much reduced due to missing of latent heat [20]. Therefore, it is necessary to explore a novel material with a large ΔT accompanied by wide ΔT_{span} .

Enlightened by high-entropy alloys (HEA) in metallurgy, high-entropy ceramics (HECs) have drawn increasing attractions due to their unique structure and performances [21–23]. Introducing high configurational entropy opens up an exciting and numerous unexpected performances. High-entropy oxide (HEO) ($\text{Mg}_{0.2}\text{Zn}_{0.2}\text{Cu}_{0.2}\text{Co}_{0.2}\text{Ni}_{0.2}\text{O}$) ceramic was reported by Rost et al. [24], which provided a

guideline for property engineering via deliberately designing configurational disorder. Afterward, various HEO ceramics are synthesized, such as spinel-structure ($\text{Co}_{0.2}\text{Cr}_{0.2}\text{Fe}_{0.2}\text{Mn}_{0.2}\text{Ni}_{0.2}$) $_3\text{O}_4$ [25], fluorite-oxide ($\text{Ce}_{0.2}\text{Zr}_{0.2}\text{Hf}_{0.2}\text{Sn}_{0.2}\text{Ti}_{0.2}$) O_2 with low thermal conductivity [26] and perovskite-structure $\text{Sr}(\text{Zr}_{0.2}\text{Sn}_{0.2}\text{Ti}_{0.2}\text{Hf}_{0.2}\text{Nb}_{0.2})\text{O}_3$ [27]. The HEO ceramics have also shown peculiar performances in colossal dielectric relaxation [28], superconductivity [29] and catalytic [30, 31]. However, research on ECE in HEO is scarce thus far. Pu et al. reported a kind of $(\text{Na}_{0.2}\text{Bi}_{0.2}\text{Ba}_{0.2}\text{Sr}_{0.2}\text{Ca}_{0.2})\text{TiO}_3$ ceramic, which demonstrated possible applications in solid-state refrigeration and energy-storage devices [32]. Du et al. also synthesized $\text{Ba}(\text{Ti}_{1/6}\text{Sn}_{1/6}\text{Zr}_{1/6}\text{Hf}_{1/6}\text{Nb}_{1/6}\text{Ga}_{1/6})\text{O}_3$ ceramic with substitution of six different cations at *B*-site and phase formation and dielectric properties in this ceramic were analyzed [33].

Inspired by these researches, high-entropy perovskite oxides with six components at *A*-site is fabricated for exploring possible peculiar performances. In this work, two kinds of high-entropy perovskite oxides $(\text{Bi}_{1/6}\text{Na}_{1/6}\text{Sr}_{1/6}\text{Ba}_{1/6}\text{Pb}_{1/6}\text{Ca}_{1/6})\text{TiO}_3$ (BNSBPC) and $(\text{Bi}_{1/6}\text{La}_{1/6}\text{Na}_{1/6}\text{K}_{1/6}\text{Sr}_{1/6}\text{Ba}_{1/6})\text{TiO}_3$ (BLNKSB) with equimolar proportions of six elements at *A*-site are firstly reported. These materials have a configurational entropy (ΔS_{config}) of 1.79R ($\Delta S_{\text{config}} = -R \sum_{i=1}^N x_i \ln x_i$, where *R* is the gas constant of 8.314 J mol⁻¹ K⁻¹, x_i is the molar concentration of each element), which is higher than 1.5R (minimal value of high entropy in definition) [34]. The influence of *A*-site multi-element incorporations on phase/local structure, dielectric/ferroelectric properties and ECE are discussed in detail.

Experimental section

Synthesis

$(\text{Bi}_{1/6}\text{Na}_{1/6}\text{Sr}_{1/6}\text{Ba}_{1/6}\text{Pb}_{1/6}\text{Ca}_{1/6})\text{TiO}_3$ and $(\text{Bi}_{1/6}\text{La}_{1/6}\text{Na}_{1/6}\text{K}_{1/6}\text{Sr}_{1/6}\text{Ba}_{1/6})\text{TiO}_3$ ceramics were prepared through a conventional solid-state method by using high purity raw chemicals Bi_2O_3 ($\geq 99\%$), Na_2CO_3 ($\geq 99.8\%$), SrCO_3 ($\geq 99\%$), BaCO_3 ($\geq 99\%$), PbO ($\geq 99\%$), CaCO_3 ($\geq 99\%$), K_2CO_3 ($\geq 99\%$), La_2O_3 ($\geq 99.99\%$) and TiO_2 ($\geq 98\%$). Na_2CO_3 and K_2CO_3 raw materials were dried for 12 h at 150 °C in advance for removing water absorption. Firstly, raw

chemicals were mixed in stoichiometric ratios and ball milled for 18 h. The resultant powders were dried at 100 °C for 12 h. Then, BNSBPC and BLNKSB powders were calcined at various temperatures for four hours to obtain a single-phase compound. After calcination, powders were ball-milled again for 15 h, and then dried powders were ground with 8 wt.% PVA as a binder. The weight ratio of PVA to powder is about 1:4. The granulated powders were pressed into pellets with 10 mm in diameter and 1 mm in thickness with cold-isostatic pressure of 6 MPa. After removing the PVA binder, compacted pellets were sintered at 1260 °C with soaking time of three hours. The heating rate is 3 °C min⁻¹ and they were cooled with furnace when sintering was finished. The polished pellets for both compositions are about 0.4 mm in thickness with an area of ~ 59.4 mm².

Measurement

The lattice structure of HECs was measured by X-ray diffractometer (XRD, Rigaku Smart-lab Beijing Co, Beijing, China). The sample morphology was observed by a scanning electron microscope (SEM, Regulus 8230; Hitachi Co, Tokyo, Japan). Sample surface was polished and thermally etched at 1150 °C for 30 min. Archimedes method was used to measure samples' density. The density of BNSBPC and BLNKSB ceramic was measured to be 5.73 g cm⁻³ and 5.48 g cm⁻³, respectively. Temperature-dependent dielectric properties were measured by Wayne Kerr 6500B impedance analyzer (Wayne Kerr Electronic Instrument Co., Shenzhen, China) with a Partulab DMS-2000 apparatus (Partulab Technology Co, Wuhan, China) in the frequency range of 0.1 kHz ~ 1 MHz. Temperature-dependent polarization–electric field hysteresis loops (*P*–*E*) were measured with frequency of 1 Hz by a ferroelectric test system (Precision LC, Radiant Technologies, Inc. Albuquerque, NM) with Delta-9023 device. Specific heat capacity *C_p* was measured by a differential scanning calorimeter (DSC, TA Instruments Q2000, USA). Raman spectroscopy was measured by Renishaw Raman microscope with a 532 nm laser and a temperature controller (Linkam THMSE 600). Direct ECE was measured by using a home-made adiabatic calorimeter, which can be referred to [35, 36].

Results and discussion

To investigate the phase formation and lattice structure, XRD patterns of BNSBPC and BLNKSB powders calcined at various temperatures are displayed in Fig. 1a and c. XRD patterns show that secondary phase appears at a lower calcined temperature and intensity of miscellaneous peaks decrease gradually with increasing temperature. Decrease in second-phase peak intensity with rising temperature is due to the decreased concentration of nonperovskite-structure composition. When temperature reaches 1193 K, BNSBPC powders form a single-phase solid solution, while the BLNKSB calcined powders show absence of secondary phase until 1273 K. This phenomenon is explained as both entropy and enthalpy drive the material to form a stable single-phase structure [32]. Decrease in entropy and increase in enthalpy can reduce Gibbs free energy and thereby enhancing thermal stability for HEC system. Considering the formation of second phase and easy volatilization of Bi/Pb/Na/K element at low/high temperature respectively, the calcined temperature is determined to be 1193 K and 1273 K for BNSBPC and BLNKSB systems. The experimental XRD patterns for crushed pellets are shown in Fig. 1b and d, which demonstrates the formation of pure perovskite structure. To get in-depth understanding of phase structure, Rietveld refinement of XRD patterns are performed. The experimental, calculated and different profiles of BNSBPC and BLNKSB composition are shown by selecting models of tetragonal (T) phase with space groups *P4mm* and cubic (C) phase with space groups *Pm* $\bar{3}$ *m*, respectively. The goodness of fit *R_{wp}* and *R_p* is lower than 15%, which indicates that fitting results are credible. The insets in Fig. 1b and d show the lattice structure of T and C phase for BNSBPC and BLNKSB, respectively. Furthermore, Jiang et al. reported that tolerance factor (~ 1) was perhaps a necessary condition to form a single phase in high-entropy perovskite materials [37]. Tolerance factor is calculated by using the following formula [38]:

$$t = \frac{R_A + R_O}{\sqrt{2}(R_B + R_O)} \quad (1)$$

where *R_A*, *R_B*, *R_O* are the effective ionic radii of *A*-site cation, *B*-site cation and oxygen anion, respectively. Tolerance factor in both HECs are calculated to be

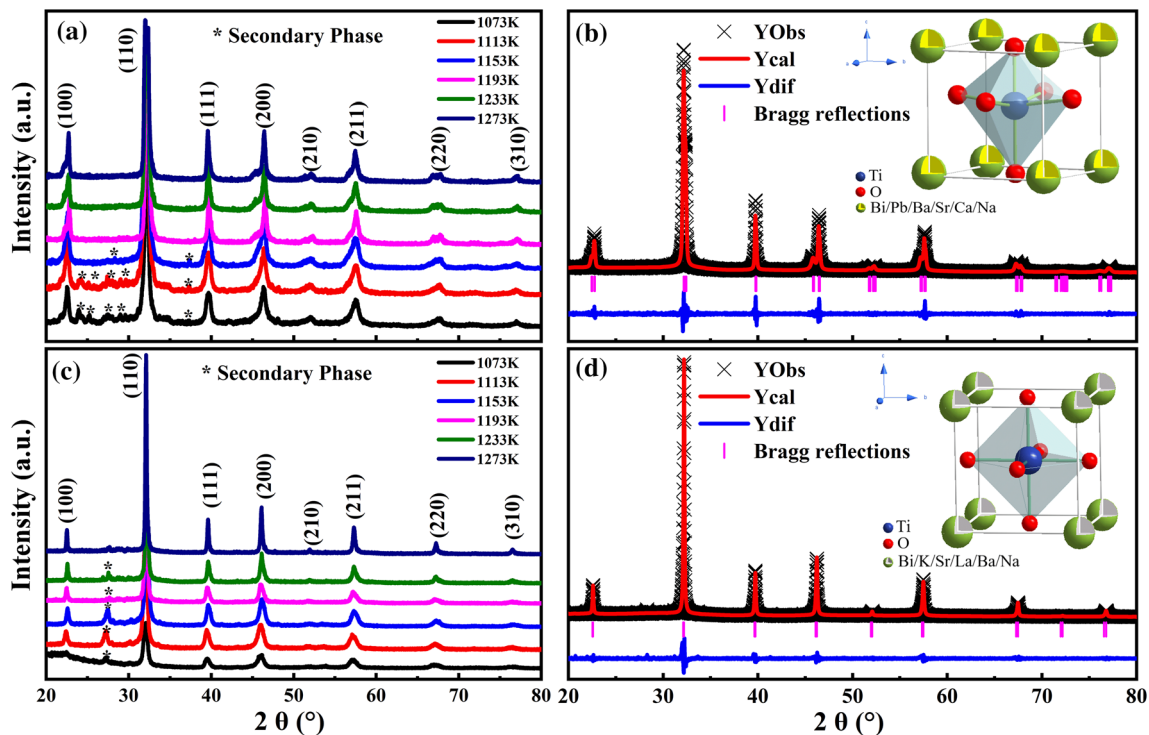


Figure 1 XRD patterns of calcined powders at various temperatures ranging from 1073 to 1273 K for (a) BNSBPC and (c) BLNKSB. Rietveld refinement patterns of (b) BNSBPC and (d) BLNKSB samples with lattice-structure illustrations in their insets, respectively (The black crosses represent the observed data

for corresponding crushed pellets, red lines are the calculated profiles, and blue lines are the difference between the observed and calculated diffraction patterns; the vertical ticks indicate the peak position of each phase).

1.006, which further confirms that the easier formation of a single-phase high-entropy ceramics.

Figure 2 shows the surface morphology of thermally-etched BNSBPC and BLNKSB ceramics with corresponding elemental mapping. Obviously, both samples exhibit dense microstructures with absence of pores and voids, as shown in Fig. 2a and h. Besides, grain size in BNSBPC ceramic ($\sim 1.29 \mu\text{m}$) is to some extent larger than that of BLNKSB one ($\sim 0.82 \mu\text{m}$). The elemental mapping images of BNSBPC and BLNKSB samples demonstrate that all A-site elements are homogeneously distributed (Fig. 2b–g and Fig. 2i–n).

Temperature dependence of dielectric constant (ϵ_r) and loss tangent ($\tan\delta$) for BNSBPC and BLNKSB ceramics are shown in Fig. 3a and c. As shown, maximal dielectric constant (ϵ_m) of BNSBPC ceramic slightly decreases with increasing frequency and the temperature corresponding to ϵ_m (T_m) has weak relationship with frequency. It is usually considered to be an intermediate state between normal and relaxor ferroelectrics [39]. Interestingly, this

composition also possesses a spontaneous ferroelectric–relaxor phase transition at ~ 403 K. On the contrary, T_m and ϵ_m value in BLNKSB ceramic distinctly depends on frequency, in which T_m increases and ϵ_m decreases with increasing frequency, as shown in Fig. 3c. The BLNKSB system is denoted as typical relaxor ferroelectric [40]. To further describe the degree of relaxation, a power law is adopted [41, 42]:

$$\frac{\epsilon_m}{\epsilon} = 1 + \frac{(T - T_m)^\gamma}{2\delta_c^2} \quad (1 \leq \gamma \leq 2) \quad (2)$$

where γ and δ_c are degree of relaxation and broadening parameter, respectively. The parameter γ reveals phase transition character: The system is an ideal normal ferroelectric as $\gamma = 1$ and an ideal relaxor as $\gamma = 2$. ϵ_m is dielectric constant at T_m . The dielectric curves for two samples above T_m are fitted, as shown in the inset of Fig. 3a–c. The parameter γ are fitted to be 1.59 and 1.68 for BNSBPC and BLNKSB ceramics, respectively. This confirms that both ceramics have a diffuse phase transition (DPT)

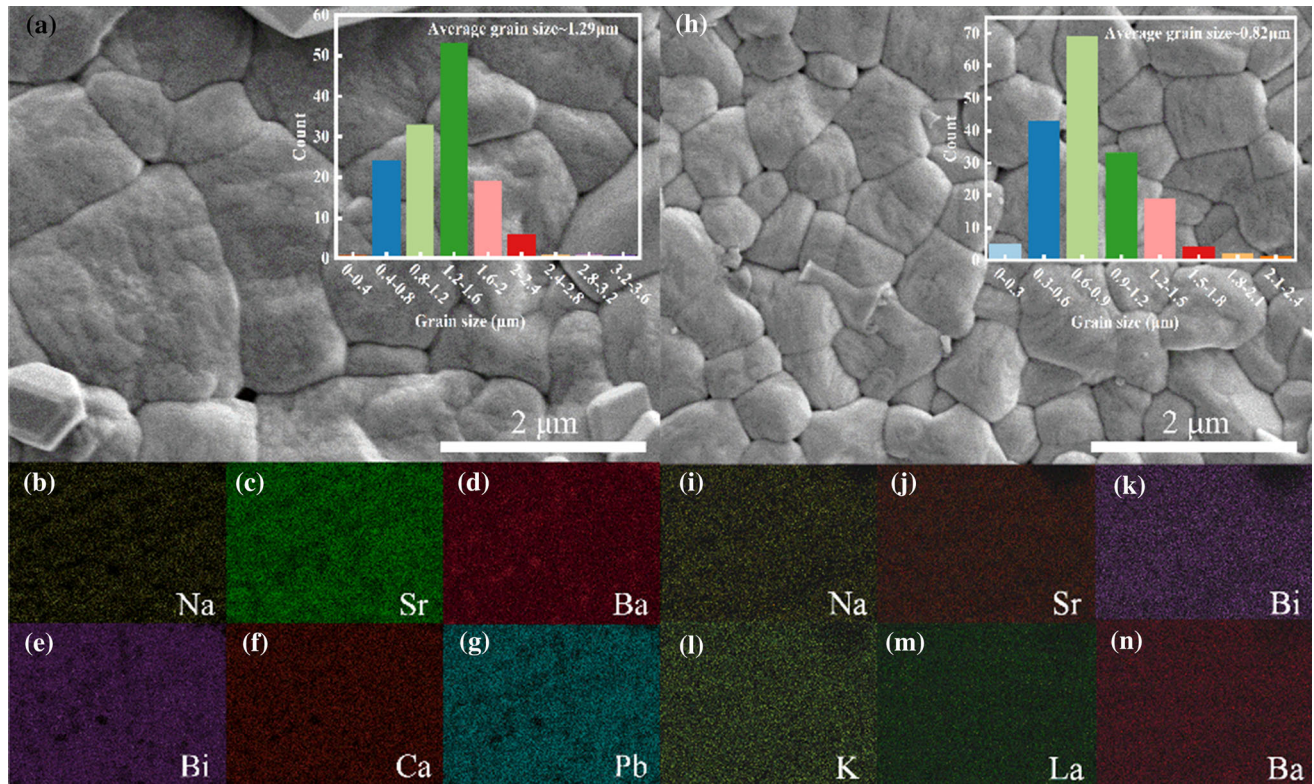


Figure 2 SEM and EDS mapping images of (a–g) BNSBPC and (h–n) BLNKSB samples.

behavior. Interestingly, the relaxor degree of BNSBPC is less than that of BLNKSB. Though incorporation of other cations induces local random field, BNSBPC behaves like a normal ferroelectric material, which is probably due to a strong hybridization between Pb 6 s and O 2p orbitals. Therefore, the BLNKSB ceramic is a relaxor ferroelectric material while the BNSBPC one is classified as a relaxor-like ferroelectric material [43].

The relaxation behavior is usually related with polar nanoregions (PNRs) [36]. At high temperature, relaxors possess non-polar paraelectric (PE) phase and then transform into an ergodic relaxor (ER) state during cooling, in which PNRs appear in this process. The dynamics of PNRs slow down and their size grows and finally freeze into a nonergodic state (NER) at freezing temperature (T_f). The T_f is obtained by using Vogel–Fulcher (V–F) law [44]:

$$f = f_0 \exp \left[- \frac{E_a}{k(T_m - T_f)} \right] \tag{3}$$

where f_0 is attempt frequency, E_a is activation energy, T_f is static freezing temperature and k is Boltzmann constant. Figure 3b shows the V–F fitting for BLNKSB

ceramic and the T_f is fitted to be 111 K. The f_0 value is about 5.83×10^{14} Hz, which is an order higher than that of its upper physical limit ($\sim 10^{12} - 10^{13}$) [45]. This indicates V–F law is unsuitable for interpreting relaxation behaviors for BLNKSB system. Interestingly, a parameter p is adopted to characterize the dielectric relaxation strength (DRS) in relaxor ferroelectric, which has been introduced by Cheng et al. [45]:

$$\omega = \omega_0 \exp \left(- \frac{T_0}{T_m} \right)^p \tag{4}$$

where ω_0 is attempt frequency and T_0 is the temperature of activation energy. Figure 3d shows the fitting result and the p^{-1} value is calculated to be 0.34, which indicates the BLNKSB system is probably a Debye medium state. In Debye medium, there is no interaction between dipoles and they can be frozen only at absolute zero temperature theoretically [45].

In-situ temperature-dependent Raman spectra are performed to clarify the local structure evolution, as shown in Fig. 4(a, c). All Raman spectra are corrected by using Bose–Einstein temperature factor [20]. The corrected Raman intensity is calculated by the formula:

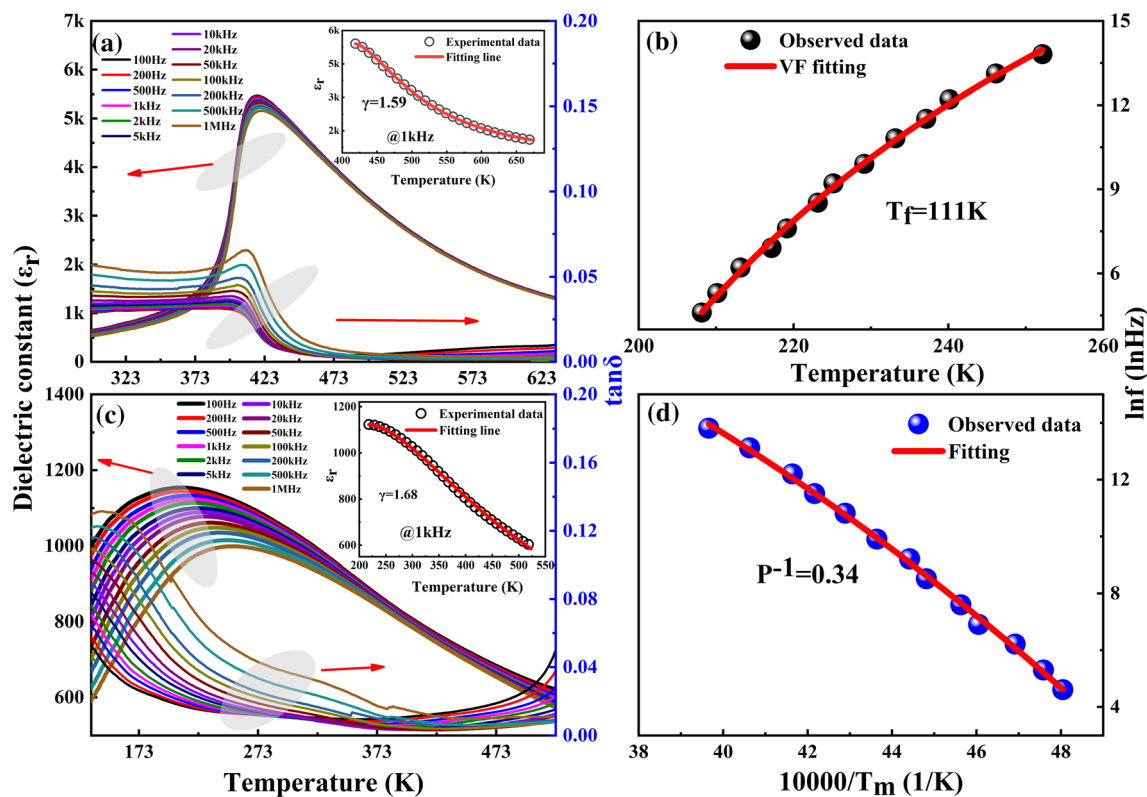


Figure 3 Temperature dependent dielectric constant (ϵ_r) and loss tangent ($\tan\delta$) of (a) BNSBPC and (c) BLNKSB ceramics. The insets in (a) and (c) show the fitting by power law at 1 kHz,

$$I_c(\omega) = I_m(\omega)/[n(\omega, T) + 1] \quad (5)$$

where $I_c(\omega)$ is calculated Raman intensity and $n(\omega, T) = [1/\exp(\frac{\hbar\omega}{kT}) - 1]$ is temperature factor. Obviously, all Raman spectra are broad and diffuse, which is due to random occupations of various cations at A-site. In general, Raman spectra can be divided into four regions within 100–1000 cm^{-1} : (a) mixed A-site vibrations within 100–200 cm^{-1} ; (b) Ti–O bond vibrations in the range of 200–400 cm^{-1} ; (c) TiO_6 octahedral vibrations within 400–700 cm^{-1} (d) the region above 700 cm^{-1} is correlated with the A1 and E overlapping modes [20, 46–49]. To analyze temperature-dependent phase transition, Raman spectra are deconvoluted into Lorentzian peaks from 100 cm^{-1} to 700 cm^{-1} to obtain the band position and full width at half maximum (FWHM). As well known, analysis of band position and FWHM evolution in Raman spectra can deeply understand the local structure changing as temperature increases. The deconvolution of peaks is shown in the bottom of Fig. 4b and d for BNSBPC and BLNKSB system, respectively.

respectively; (b) Vogel–Fulcher fitting of BLNKSB ceramics; (d) The fitting parameter p for BLNKSB ceramic.

Since 200–400 cm^{-1} wavenumber region is associated with Ti–O bands vibrations, it is usually selected to probe phase transitions in perovskite-type ceramics [49]. The evolution of band position and FWHM within 200–400 cm^{-1} is plotted in Fig. 5. Obviously, the wavenumber and FWHM exhibit a discontinuity at 403 K for BNSBPC composition (as highlighted by the shadow area), which signifies the appearance of phase transition. This is also in accordance with the spontaneous ferroelectric–relaxor phase transition temperature (see dielectric curves). The missing of anomaly in wavenumbers and FWHM evolution within 93 ~ 313 K demonstrates an absence of ferroelectric–relaxor phase transition. Therefore, phase transition character in BLNKSB composition is strikingly different to that of BNSBPC.

Figure 6(a–b, d–e) shows the temperature dependence of polarization–electric field (P – E) hysteresis loops and current density–electric field (J – E) loops for BNSBPC and BLNKSB ceramics ($E = 60 \text{ kV cm}^{-1}$). As shown in Fig. 6a, BNSBPC sample has a relatively slim P – E loop at high temperature and gradually

Figure 4 In-situ temperature dependent Raman spectra for (a) BNSBPC ceramic in the temperature range of 293–533 K and (c) BLNKSB ceramic in the temperature range of 93–313 K. Deconvolution of Raman spectra are shown in the bottom of (b) BNSBPC ceramic at 293 K and (d) BLNKSB ceramic at 93 K.

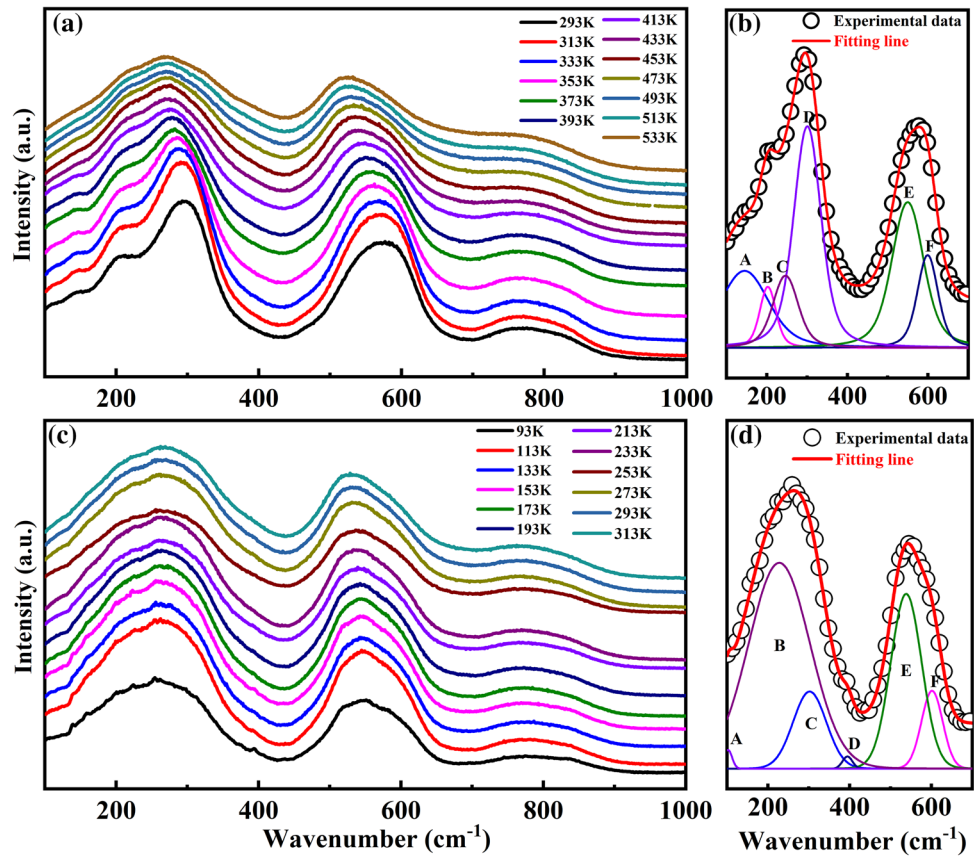
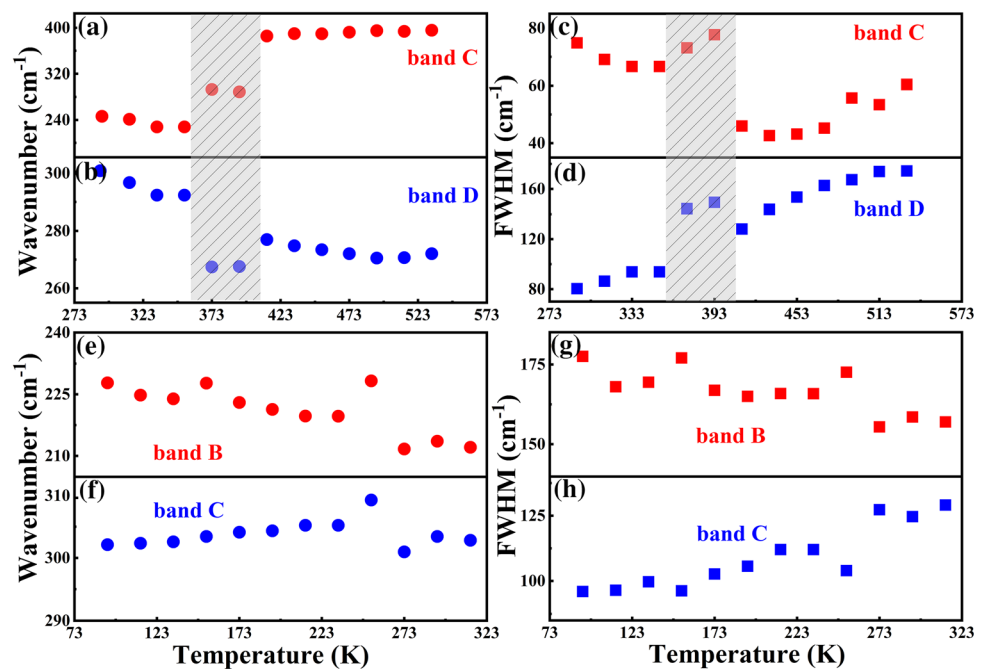


Figure 5 Temperature-dependent wavenumber and FWHM of selected modes for (a–d) BNSBPC and (e–h) BLNKSB ceramic.



transforms to a slanted shape and finally to a square shape with decreasing temperature. As well known, thermal agitation tends to destroy long-range polar

correlations into fragmented nanodomains (ND) and finally PNRs [20]. The ferroelectric state revives with decreasing temperature due to re-connections of ND

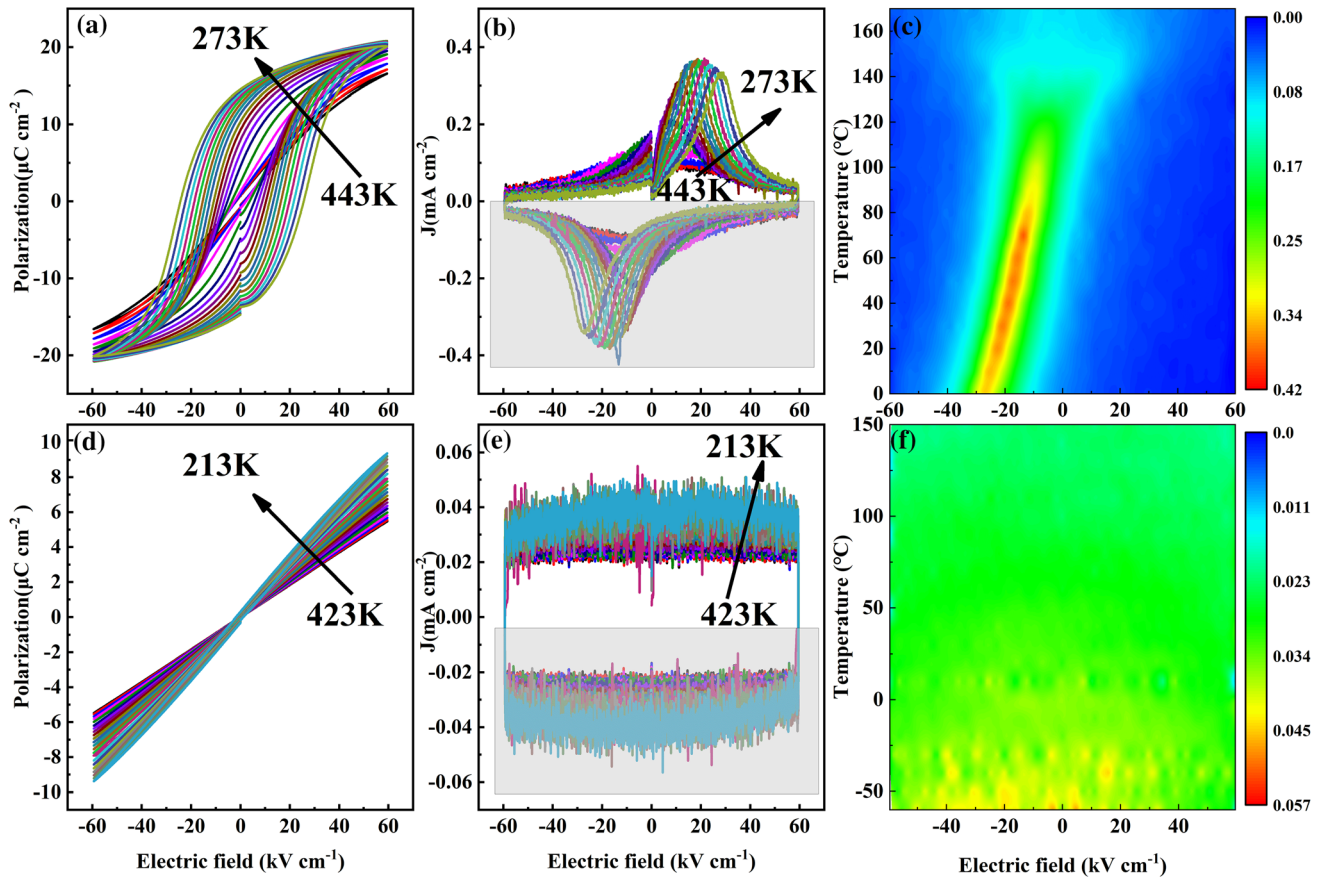


Figure 6 P - E loops, J - E loops and the contour map of absolute current density value as a function of electric field (extracted from the shadow section): (a–c) BNSBPC and (d–f) BLNKSB ceramic.

and PNRs. Combined with J - E loops (Fig. 6b) and contour map of absolute J - E (Fig. 6c), the single current peak is observed when the temperature decreases to 403 K, which demonstrates a relaxor-ferroelectric phase transition. However, ferroelectric property in BLNKSB ceramic is quite different, as shown in Fig. 6e, f. P - E loops are always slim within the temperature range of 213 ~ 423 K accompanied by rectangle J - E loops, which means an absence of domain switching under electric field. Notably, maximal polarization (P_{\max}) increases gradually with decreasing temperature for both samples since the reduction of thermal disturbance [14].

The indirect method is used to calculate temperature change according to Maxwell relation, which is expressed by the following equation:

$$\Delta T = -\frac{T}{\rho C_p} \int_{E_1}^{E_2} \left(\frac{\partial P}{\partial T} \right)_E dE \quad (6)$$

where ρ is ceramic density, C_p is specific heat capacity and its evolution as temperature increases is

shown in Fig. 7a, b. In contrast to BLNKSB ceramic, the gentle heat capacity peak near the Curie temperature illustrates relaxor-like behaviors for BNSBPC ceramics [50]. This may signal that BNSBPC composition is in an intermediate state of first-order and second-order phase transition. E_1 and E_2 is initial and final electric-field strength, respectively. The value of $(\partial P/\partial T)_E$ is gained from a seven-order polynomial fitting of raw P_{\max} - T (extracted from Fig. 6(a, d)) at various external electric fields, as shown in Fig. 7c, d. Figure 7e, f shows profiles of adiabatic temperature change versus temperature (ΔT - T) under different electric fields. Obviously, ΔT of both samples increases with increasing electric field strength from $E = 1 \sim 6$ kV mm⁻¹. Interestingly, ΔT is found to increase first and then decrease as temperature surpasses to 413 K for BNSBPC ceramic. As shown in Fig. 7e, the ΔT_{\max} is 0.63 K at 413 K under $E = 6$ kV mm⁻¹, which is comparable to other systems [7, 14, 17, 27, 32, 51]. Since distinct entropy change takes place across the phase

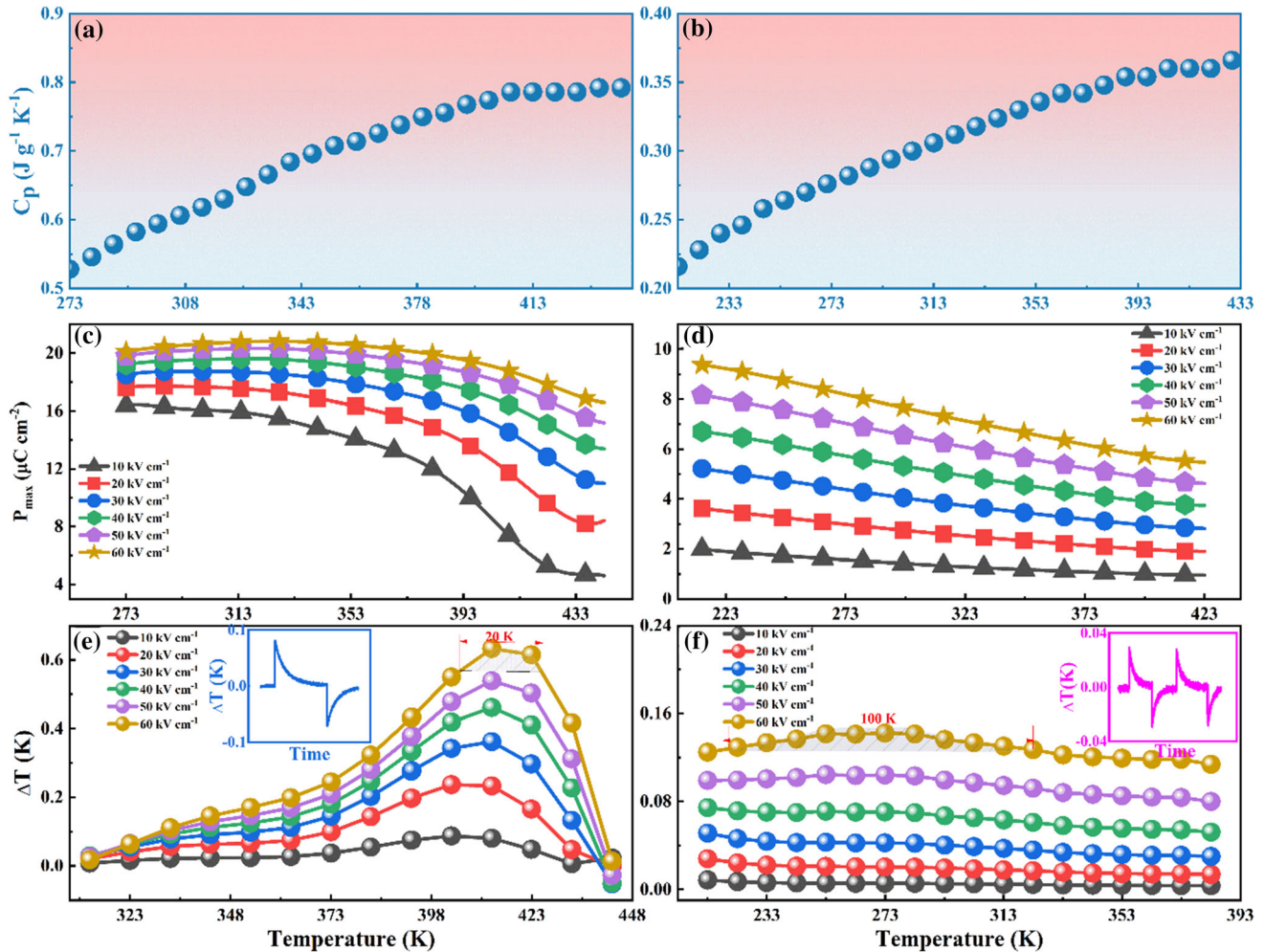


Figure 7 Specific heat capacity C_p as a function of temperature: (a) BNSBPC ceramic; (b) BLNKSB ceramic. Maximal polarization versus temperature ($P_{max}-T$) for (c) BNSBPC and (d) BLNKSB at various electric field. ECE versus temperature

($\Delta T-T$) at different electric fields by indirect method for (e) BNSBPC and (f) BLNKSB ceramic. The insets of (e–f) show the ΔT measured by direct method under 60 kV cm^{-1} at room temperature, respectively.

transition, high ECE is hardly maintained over a wide temperature window [14]. The ECE peak occurs in the vicinity of ferroelectric–relaxor phase transition and the ΔT_{span} (defined as $\pm 10\%$ variation of ΔT_{max}) is only 20 K, which limits its application in solid-state cooling devices. In contrast, BLNKSB ceramic possesses $\Delta T_{max} \sim 0.14 \text{ K}$ and an ultrawide temperature span ($\sim 100 \text{ K}$) ranging from 223 to 323 K, as shown in Fig. 7f, which is superior to other lead-free ceramics [14, 17, 52, 53]. The large ΔT_{span} is related to the Debye medium character of BLNKSB since an absence of phase transition. The directly measured room-temperature ECE in both ceramics are shown in insets of Fig. 7(e, f) ($E = 60 \text{ kV cm}^{-1}$). As electric field is applied, there appears an upward exothermic peak, and when electric field is removed, there is a

downward endothermic peak. This presents an obvious positive ECE characteristic. ΔT is about 0.08 K for BNSBPC and 0.03 K for BLNKSB ceramics at room temperature, which is slightly different to that of indirect method and likely because of the hysteretic response for calorimeter [53]. As a matter of fact, both indirect and direct method are adopted to calculate the ECE in ferroelectric materials. Notably, the variation trend matches well for both methods though ECE value may exist some differences [13, 14, 53].

The electrocaloric strength (dT/dE) is an important parameter to estimate ECE properties under electric field. Based on the thermodynamic theory, Lu et al. obtained the electrocaloric strength (dT/dE) equation [54, 55]:

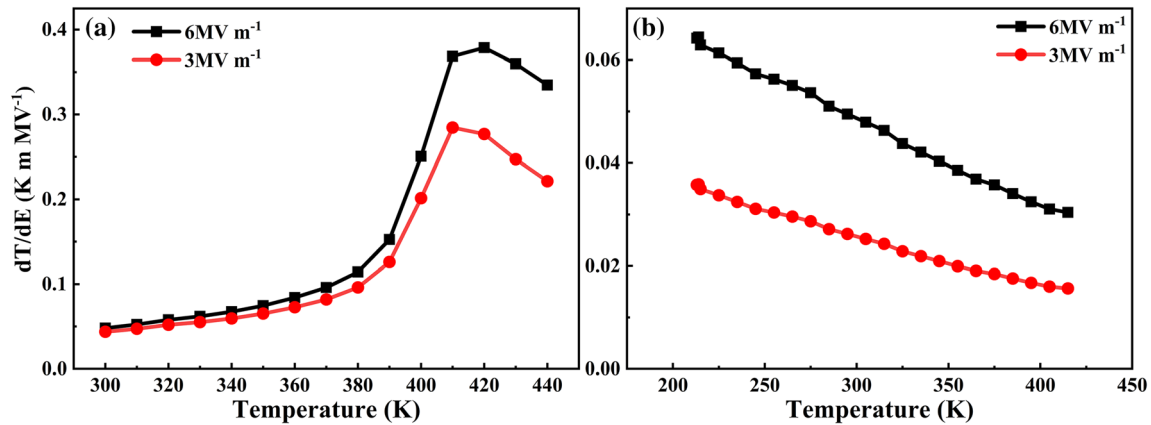


Figure 8 Calculated electrocaloric strengths (dT/dE) as a function of temperature at electric field of 3 MV m^{-1} and 6 MV m^{-1} for (a) BNSBPC and (b) BLNKSb ceramics.

$$\frac{dT}{dE} = \frac{\beta \varepsilon_0 \varepsilon_r T P}{\rho C_v} \quad (7)$$

where β is the phenomenological coefficient ($\sim 4.71 \times 10^5 \text{ K}^{-1}$ and $3.83 \times 10^5 \text{ K}^{-1}$ for BNSBPC and BLNKSb, respectively), ε_0 is vacuum dielectric constant ($\sim 8.85 \times 10^{-12} \text{ F m}^{-1}$), ε_r is relative dielectric constant and C_v is the specific heat per unit volume. Figure 8 shows the dT/dE versus temperature at 3 MV m^{-1} and 6 MV m^{-1} for BNSBPC and BLNKSb ceramics, respectively. With increasing electric field, the dT/dE also show an increase. Obviously, dT/dE first increases and then decreases for BNSBPC ceramic, and maximal dT/dE is $0.379 \text{ K m MV}^{-1}$ near 420 K . In terms of BLNKSb ceramics, dT/dE gradually decreases with increasing temperature and maximal dT/dE is $0.064 \text{ K m MV}^{-1}$ near 215 K . The calculated electrocaloric strength at room temperature ($\sim 0.048 \text{ K m MV}^{-1}$ and $0.049 \text{ K m MV}^{-1}$) for BNSBPC and BLNKSb ceramics are larger than that of practical measured values ($\sim 0.013 \text{ K m MV}^{-1}$ and $0.005 \text{ K m MV}^{-1}$), which maybe due to the heat dissipation in the ECE measurement.

Conclusion

In summary, we have successfully synthesized two kinds of pure-phase high-entropy ceramics with perovskite structure. The BNSBPC ceramic possesses a tetragonal structure with relaxor-like dielectric behaviors and the BLNKSb one has a cubic phase with Debye medium relaxation. The dielectric and

Raman spectra analysis also verify the phase transition for both ceramics. The BNSBPC ceramic shows $\Delta T_{max} = 0.63 \text{ K}$ with a relatively narrow $\Delta T_{span} \sim 20 \text{ K}$ under $E = 60 \text{ kV cm}^{-1}$, while the BLNKSb exhibits excellent temperature stability with $\Delta T_{span} = 100 \text{ K}$ and $\Delta T_{max} = 0.14 \text{ K}$. The high temperature stability for the BLNKSb ceramic is conducive to cooling device applications, and its ECE value deserves to be further improved yet. This work guides us to further explore high-performance ECE in HEC materials and also opens a way to developing novel materials in solid-state refrigeration applications.

Acknowledgements

This work was supported by Anhui Provincial Natural Science Foundation (No. 2008085QE205), Anhui Provincial higher-education Natural Science research project (KJ2020A0019), the Open Project Program of Guangdong Provincial Key Laboratory of Electronic Functional Materials and Devices, Huizhou University (No. EFMD2020004Z), Guangxi Key Laboratory of Information Materials (Guilin University of Electronic Technology, No. 201006-K) and the National Natural Science Foundation of China (Nos. 51872001 and 51772211).

Declarations

Conflict of interest The authors declare that they have no conflict of interest.

References

- [1] Ma RJ, Zhang ZY, Tong KW, Huber D, Kornbluh R, Ju YS, Pei QB (2017) Highly efficient electrocaloric cooling with electrostatic actuation. *Science* 357(6356):1130–1134
- [2] Valant M (2012) Electrocaloric materials for future solid-state refrigeration technologies. *Prog Mater Sci* 57(6):980–1009
- [3] Mischenko AS, Zhang Q, Scott JF, Whatmore RW, Mathur ND (2006) Giant electrocaloric effect in thin-film $\text{PbZr}_{0.95}\text{Ti}_{0.05}\text{O}_3$. *Science* 311(5765):1270–1271
- [4] Hagberg J, Uusimäki A, Jantunen H (2008) Electrocaloric characteristics in reactive sintered $0.87\text{Pb}(\text{Mg}_{1/3}\text{Nb}_{2/3})\text{O}_3$ - 0.13PbTiO_3 . *Appl Phys Lett* 92(13):132909
- [5] Lu B, Jian XD, Lin XW, Yao YB, Tao T, Liang B, Luo HS, Lu SG (2020) Enhanced electrocaloric effect in single crystals via direct measurement $0.73\text{Pb}(\text{Mg}_{1/3}\text{Nb}_{2/3})\text{O}_3$ - 0.27PbTiO_3 . *Curr Comput-Aided Drug Des* 10(6):451
- [6] Jian XD, Lu B, Li DD, Yao Y-B, Tao T, Liang B, Guo JH, Zeng Y-J, Chen JL, Lu SG (2018) Direct measurement of large electrocaloric effect in $\text{Ba}(\text{Zr}_x\text{Ti}_{1-x})\text{O}_3$ Ceramics. *ACS Appl Mater Interfaces* 10(5):4801–4807
- [7] Li JN, Zhang DW, Qin SQ, Li TY, Wu M, Wang D, Bai Y, Lou XJ (2016) Large room-temperature electrocaloric effect in lead-free $\text{BaHf}_x\text{Ti}_{1-x}\text{O}_3$ ceramics under low electric field. *Acta Mater* 115:58–67
- [8] Luo ZD, Zhang DW, Liu Y, Zhou D, Yao YG, Liu CQ, Dkhil B, Ren XB, Lou XJ (2014) Enhanced electrocaloric effect in lead-free $\text{BaTi}_{1-x}\text{Sn}_x\text{O}_3$ ceramics near room temperature. *Appl Phys Lett* 105(10):102904
- [9] Bai Y, Han X, Ding K, Qiao LJ (2013) Combined effects of diffuse phase transition and microstructure on the electrocaloric effect $\text{Ba}_{1-x}\text{Sr}_x\text{TiO}_3$ in ceramics. *Appl Phys Lett* 103(16):162902
- [10] Han F, Bai Y, Qiao LJ, Guo D (2016) A systematic modification of the large electrocaloric effect within a broad temperature range in rare-earth doped BaTiO_3 ceramics. *J Mater Chem C* 4(9):1842–1849
- [11] Weyland F, Eisele T, Steiner S, Fromling T, Rossetti GA, Rodel J, Novak N (2018) Long term stability of electrocaloric response in barium zirconate titanate. *J Eur Ceram Soc* 38(2):551–556
- [12] Hanani Z, Merselmiz S, Danine A, Stein N, Mezzane D, Mb A, Lahcini M, Gagou Y, Spreitzer M, Vengust D, Kutnjak Z, El Marssi M, Luk'yanchuk IA, Gouné M (2020) Enhanced dielectric and electrocaloric properties in lead-free rod-like BCZT ceramics. *J Adv Ceram* 9(2):210–219
- [13] Li JT, Bai Y, Qin SQ, Fu J, Zuo RZ, Qiao LJ (2016) Direct and indirect characterization of electrocaloric effect in (Na, K)NbO₃ based lead-free ceramics. *Appl Phys Lett* 109(16):162902
- [14] Yang JL, Zhao Y, Lou XJ, Wu JG, Hao XH (2020) Synergistically optimizing electrocaloric effects and temperature span in KNN-based ceramics utilizing a relaxor multiphase boundary. *J Mater Chem C* 8(12):4030–4039
- [15] Wang XJ, Wu JG, Dkhil B, Xu BX, Wang XP, Dong GH, Yang G, Lou XJ (2017) Enhanced electrocaloric effect near polymorphic phase boundary in lead-free potassium sodium niobate ceramics. *Appl Phys Lett* 110(6):063904
- [16] Tao H, Yang JL, Lv X, Hao XH, Wu JG (2019) Electrocaloric behavior and piezoelectric effect in relaxor NaNbO_3 -based ceramics. *J Am Ceram Soc* 102(5):2578–2586
- [17] Yu Y, Gao F, Weyland F, Du HL, Jin L, Hou L, Yang ZT, Novak N, Qu SB (2019) Significantly enhanced room temperature electrocaloric response with superior thermal stability in sodium niobate-based bulk ceramics. *J Mater Chem A* 7(19):11665–11672
- [18] Turki O, Slimani A, Seveyrat L, Sebald G, Perrin V, Sassi Z, Khemakhem H, Lebrun L (2016) Structural, dielectric, ferroelectric, and electrocaloric properties of 2% Gd_2O_3 doping ($\text{Na}_{0.5}\text{Bi}_{0.5}$)(0.94) $\text{Ba}_{0.06}\text{TiO}_3$ ceramics. *J Appl Phys* 120(5):054102
- [19] Weyland F, Acosta M, Koruza J, Breckner P, Rodel J, Novak N (2016) Criticality: concept to enhance the piezoelectric and electrocaloric properties of ferroelectrics. *Adv Func Mater* 26(40):7326–7333
- [20] Li F, Li J, Zhai J, Shen B, Li S, Zhou M, Zhao K, Zeng H (2018) Influence of structural evolution on electrocaloric effect in $\text{Bi}_{0.5}\text{Na}_{0.5}\text{TiO}_3$ - SrTiO_3 ferroelectric ceramics. *J Appl Phys* 124(16):164108
- [21] Miracle DB, Senkov ON (2017) A critical review of high entropy alloys and related concepts. *Acta Mater* 122:448–511
- [22] Oses C, Toher C, Curtarolo S (2020) High-entropy ceramics. *Nat Rev Mater* 5(4):295–309
- [23] Djenadic R, Sarkar A, Clemens O, Loho C, Botros M, Chakravadhanula VSK, Kubel C, Bhattacharya SS, Gandhif AS, Hahn H (2017) Multicomponent equiatomic rare earth oxides. *Mater Res Lett* 5(2):102–109
- [24] Rost CM, Sachet E, Borman T, Moballeggh A, Dickey EC, Hou D, Jones JL, Curtarolo S, Maria JP (2015) Entropy-stabilized oxides. *Nat Commun* 6:8485
- [25] Dabrowa J, Stygar M, Mikula A, Knapik A, Mroczka K, Tejchman W, Danielewski M, Martin M (2018) Synthesis and microstructure of the (Co, Cr, Fe, Mn, Ni)₃O₄ high entropy oxide characterized by spinel structure. *Mater Lett* 216:32–36

- [26] Chen K, Pei X, Tang L, Cheng H, Li Z, Li C, Zhang X, An L (2018) A five-component entropy-stabilized fluorite oxide. *J Eur Ceram Soc* 38(11):4161–4164
- [27] Ge PZ, Tang XG, Liu QX, Jiang YP, Li WH, Luo J (2018) Energy storage properties and electrocaloric effect of Ba_{0.65}Sr_{0.35}TiO₃ ceramics near room temperature. *J Mater Sci-Mater Electron* 29(2):1075–1081
- [28] Bérardan D, Franger S, Dragoe D, Meena AK, Dragoe N (2016) Colossal dielectric constant in high entropy oxides. *Physica Status Solidi (RRL) Rapid Res Lett* 10(4):328–333
- [29] Bérardan D, Franger S, Meena AK, Dragoe N (2016) Room temperature lithium superionic conductivity in high entropy oxides. *J Mat Chem A* 4(24):9536–9541
- [30] Chen H, Fu J, Zhang P, Peng H, Abney CW, Jie K, Liu X, Chi M, Dai S (2018) Entropy-stabilized metal oxide solid solutions as CO oxidation catalysts with high-temperature stability. *J Mater Chem A* 6(24):11129–11133
- [31] Zhai S, Rojas J, Ahlborg N, Lim K, Toney MF, Jin H, Chueh WC, Majumdar A (2018) The use of poly-cation oxides to lower the temperature of two-step thermochemical water splitting. *Energy Environ Sci* 11(8):2172–2178
- [32] Pu Y, Zhang Q, Li R, Chen M, Du X, Zhou S (2019) Dielectric properties and electrocaloric effect of high-entropy (Na_{0.2}Bi_{0.2}Ba_{0.2}Sr_{0.2}Ca_{0.2})TiO₃ ceramic. *Appl Phys Lett* 115:223901
- [33] Du Q, Yan JH, Zhang XY, Li JS, Liu XY, Zhang JR, Qi XW (2020) Phase evolution and dielectric properties of Ba(Ti_{1/6}Sn_{1/6}Zr_{1/6}Hf_{1/6}Nb_{1/6}Ga_{1/6})O₃ high-entropy perovskite ceramics. *J Mater Sci-Mater Electron* 31(10):7760–7765
- [34] Xiang HM, Xing Y, Dai FZ, Wang HJ, Su L, Miao L, Zhang GJ, Wang YG, Qi XW, Yao L, Wang HL, Zhao B, Li JQ, Zhou YC (2021) High-entropy ceramics: Present status, challenges, and a look forward. *J Adv Ceram* 10(3):385–441
- [35] Li F, Chen GR, Liu X, Zhai JW, Shen B, Zeng HR, Li SD, Li P, Yang K, Yan HX (2017) Phase-composition and temperature dependence of electrocaloric effect in lead-free Bi_{0.5}Na_{0.5}TiO₃-BaTiO₃-(Sr_{0.7}Bi_{0.2}□_{0.1})TiO₃ ceramics. *J Eur Ceram Soc* 37(15):4732–4740
- [36] Li F, Li J, Zhai J, Shen B, Li S, Zeng H (2019) Phase formation and electrocaloric effect in nonstoichiometric 0.94Bi_{0.5+x}Na_{0.5}TiO₃-0.06BaTiO₃ ceramics. *J Mater Sci-Mater Electron* 30(4):3465–3471
- [37] Jiang S, Hu T, Gild J, Zhou N, Nie J, Qin M, Harrington T, Vecchio K, Luo J (2018) A new class of high-entropy perovskite oxides. *Scripta Mater* 142:116–120
- [38] Goldschmidt VM (1926) Die Gesetze der Kristallochemie. *Naturwissenschaften* 14(21):477–485
- [39] Shvartsman VV, Kleemann W, Dec J, Xu ZK, Lu SG (2006) Diffuse phase transition in BaTi_{1-x}Sn_xO₃ ceramics: An intermediate state between ferroelectric and relaxor behavior. *J Appl Phys* 99(12):124111
- [40] Bokov AA, Ye ZG (2006) Recent progress in relaxor ferroelectrics with perovskite structure. *J Mater Sci* 41(1):31–52
- [41] Sharma P, Kumar P, Kundu RS, Juneja JK, Ahlawat N, Punia R (2015) Structural and dielectric properties of substituted barium titanate ceramics for capacitor applications. *Ceram Int* 41(10):13425–13432
- [42] Sharma P, Berwal N, Ahlawat N, Maan AS, Punia R (2019) Study of structural, dielectric, ferroelectric and magnetic properties of vanadium doped BCT ceramics. *Ceram Int* 45(16):20368–20378
- [43] Xiong W, Zhang H, Cao S, Gao F, Svec P, Dusza J, Reece MJ, Yan H (2021) Low-loss high entropy relaxor-like ferroelectrics with A-site disorder. *J Eur Ceram Soc* 41(4):2979–2985
- [44] Viehland D, Jang SJ, Cross LE, Wuttig M (1990) Freezing of the polarization fluctuations in lead magnesium niobate relaxors. *J Appl Phys* 68(6):2916–2921
- [45] Cheng ZY, Zhang LY, Yao X (1996) Investigation of glassy behavior of lead magnesium niobate relaxors. *J Appl Phys* 79(11):8615–8619
- [46] Barick BK, Mishra KK, Arora AK, Choudhary RNP, Pradhan DK (2011) Impedance and Raman spectroscopic studies of (Na_{0.5}Bi_{0.5})TiO₃. *J Phys D-Appl Phys* 44(35):8615–8619
- [47] Jiang XJ, Wang BY, Luo LH, Li WP, Zhou J, Chen HB (2014) Electrical properties of (1-x)(Bi_{0.5}Na_{0.5})TiO₃-xKNbO₃ lead-free ceramics. *J Solid State Chem* 213:72–78
- [48] Schutz D, Deluca M, Krauss W, Feteira A, Jackson T, Reichmann K (2012) Lone-pair-induced covalency as the cause of temperature- and field-induced instabilities in bismuth sodium titanate. *Adv Func Mater* 22(11):2285–2294
- [49] Haumont R, Gemeiner P, Dkhil B, Kiat JM, Bulou A (2006) Polar and chemical states at a nanometer scale in a PbSc_{1/2}Nb_{1/2}O₃-PbTiO₃ system investigated by Raman spectroscopy. *Phys Rev B* 73(10):104106
- [50] Li J, Li J, Qin S, Su X, Qiao L, Wang Y, Lookman T, Bai Y (2019) Effects of long- and short-range ferroelectric order on the electrocaloric effect in relaxor ferroelectric ceramics. *Phys Rev Appl* 11(4):044032
- [51] Wang JF, Yang TQ, Chen SC, Li G, Zhang QF, Yao X (2013) Nonadiabatic direct measurement electrocaloric effect in lead-free Ba, Ca(Zr, Ti)₃O₃ ceramics. *J Alloy Compd* 550:561–563
- [52] Zhang L, Zhao C, Zheng T, Wu J (2021) Large electrocaloric response with superior temperature stability in NaNbO₃-based relaxor ferroelectrics benefiting from the crossover region. *J Mater Chem A* 9(5):2806–2814

- [53] Li F, Li K, Long MS, Wang CC, Chen GH, Zhai JW (2021) Ferroelectric-relaxor crossover induce large electrocaloric effect with ultrawide temperature span in NaNbO_3 -based lead-free ceramics. *Appl Phys Lett* 118(4):043902
- [54] Lu SG, Li DD, Lin XW, Jian XD, Zhao XB, Yao YB, Tao T, Liang B (2020) Influence of electric field on the phenomenological coefficient and electrocaloric strength in ferroelectrics. *Acta Physica Sinica* 69(12):127701
- [55] Lu SG, Lin XW, Li J, Li DD, Yao YB, Tao T, Liang B (2021) Enhanced electrocaloric strengths at room temperature in $(\text{Sr}_x\text{Ba}_{1-x})(\text{Sn}_{0.05}\text{Ti}_{0.95})\text{O}_3$ (lead-free ceramics). *J Alloys Compd* 871:159519

Publisher's Note Springer Nature remains neutral with regard to jurisdictional claims in published maps and institutional affiliations.